LA-UR-22-22594
Accepted Manuscript

Accumulative Roll Bonding of Alloy 2205 Duplex Steel and the Accompanying Impacts on Microstructure, Texture, and Mechanical Properties

Carpenter, John S.
Savage, Daniel Jonathan
Miller, Cody
Mccabe, Rodney James
Zheng, Shijian
Coughlin, Daniel Robert
Vogel, Sven C.

To be published in: Metallurgical and Materials Transactions A

DOI to publisher's version: 10.1007/s11661-022-06897-7

Permalink to record:
http://permalink.lanl.gov/object/view?what=info:lanl-repo/lareport/LA-UR-22-22594

Accumulative Roll Bonding of Alloy 2205 Duplex Steel and the Accompanying Impacts on Microstructure, Texture, and Mechanical Properties

JS Carpenter[1*], DJ Savage[1], CA Miller[1], RJ McCabe[1], SJ Zheng[2], DR Coughlin[3], SC Vogel[1]
[1]Los Alamos National Laboratory, Los Alamos, New Mexico, United States of America 87545
[2] Tianjin Key Laboratory of Materials Laminating Fabrication and Interface Control Technology, School of Materials Science and Engineering, Hebei University of Technology, Tianjin, China, 300130
[3]United States Steel Corporation, Pittsburgh, Pennsylvania, United States of America 15219
** Corresponding author (Email: carpenter@lanl.gov)*

Keywords: Accumulative Roll Bonding, Duplex Steel, Alloy 2205, Nanograined

ABSTRACT

The mechanical and microstructural evolution of Alloy 2205 during severe plastic deformation is examined in this study. A combination of accumulative roll bonding (ARB) and cold-rolling results in the successful formation of a nanograined dual-phase microstructure of austenite and ferrite with some transformed martensite. Severe deformation to cumulative reductions of 80.5, 92.5, 95, and 97% were performed. Microscopy indicates that grain dimensions in the sheet normal direction is less than 100 nm for reductions ≥ 92.5%. Shear banding is observed at reductions ≥ 95% while twinning is only observed at reductions < 92.5%. Neutron diffraction measurements indicated the presence of martensite for reductions ≥ 95% at ~8% volume fraction. Taken in conjunction, it appears that during initial ARB processing, both slip and twinning are active plastic mechanisms. As twinning becomes exhausted, martensitic transformation, slip, and intermittent shear banding account for the active plasticity mechanisms. Material hardness saturates at 92.5% reduction, with a maximum hardness of 45 HRC. Sub-sized tensile testing confirms this approximate hardness with measurements indicating a UTS of ~1440 MPa. Texture analysis of crystal orientation distributions in the plate normal direction suggest an approximate Kurdjumov-Sachs orientation relationship at all reductions above 80% indicating stability of the orientation relationship at high strains. The intragranular structure develops a fine scale sub-grain content with increasing deformation, resulting in a continual evolution of texture up to and including 97% reduction. The final structure presents strong components of Goss and rotated cube texture in both the austenite and ferrite. This body of work aims to compare accumulative roll bonding of an industrially relevant FCC/BCC system (Alloy 2205) to historical model FCC/BCC systems such as Cu/Nb.

1.0 INTRODUCTION

Over the past several decades, exploration of nanoscale metallic composites fabricated via vapor deposition and severe plastic deformation has been undertaken. Attention was drawn to these materials initially in the 1970s-90s when several publications pointed towards the high strength that could be obtained [1-10]. Recent studies have noted advantages in properties such as high thermal stability [11-14] and irradiation resistance [15-17]. These properties were found to be associated with the close proximity of the interphase interfaces as well as their atomic structure which were shown to provide constraints on damage accumulation in these materials [18-21].

Bulk processing through accumulative roll bonding (ARB) of many composite systems [22-27] is one synthesis route that has been well-studied recently. The ARB process can be used to bond stacks of metal materials and, when repeated, can lead to large strain and reduced layer thickness [28]. The studies largely focus on model systems that can incorporate highly pure materials (Cu, Nb, Zr, V, Ta, etc.) that are expensive. Starting with sheets of highly pure, immiscible material and careful processing ensure that a layered structure is maintained so that the role of interfaces and microstructure on the achievement of these desirable properties can be studied. Cu/Nb as an example has been very well-studied [4-6, 9, 11-12] and will form the basis for some comparisons later in this paper.

In this study, commercially available duplex stainless steel (DSS) 2205 was roll bonded to create a composite type architecture using the stabilized FCC austenite and BCC ferrite components. Duplex steels, or dual-phase steels, have been shown to exhibit a wide array of characteristics that are desirable for applications requiring high strength or superior corrosion resistance [29]. In recent years, a considerable amount of research has looked into expanding these alloys for use in more demanding environments [30-33]. The intent of the roll bonding in this study was to identify whether the interfacial structure development and mechanical properties in this common material with an irregular layer pattern would compare favorably with results found in model systems using high purity materials. The duplex steel begins with a material that has BCC islands within a FCC matrix. After processing to large strains, these islands are stretched and the material creates a pseudo-layered structure where the distance between interphase interfaces in the rolling direction and transverse direction are many orders of magnitude larger than the distance between interphase interfaces in the normal direction. This layer-type structure creates a reasonable comparison with previous studies on nanolamellar metallic composites such as Cu/Nb [4-6, 9, 11-12].

It should be noted that other studies have explored duplex steels under high strains. Kiechel et. al [34] examined the texture evolution of duplex steels as a function of cold- and hot-rolling (up to 90%). This alloy behaved as one would expect for a single-phase microstructure, with components of α- and γ-fibre as well rotated cube texture in the ferrite, and a mixed brass/goss texture in the austenite [34]. However, similar work by Ryś et. al have shown no evidence of γ-fibre in ferrite up to 90% cold rolling reduction, and Hamada et. al have shown only the brass component within the austenite (up to 65% reduction) [35-37]. Along with these differences in texture evolution, several authors have seen corresponding differences in microstructural evolution and mechanical properties. Macroscopic shear bands across the ferrite/austenite interphase interface have been observed [35-36], austenite transformation into stress-induced martensite [38-40], austenite twinning, shear band formation and phase boundary sliding [39] have all been observed in nanolaminate Alloy 2205. Additionally, Akdut et. al reported no saturation of mechanical properties, up to and including 90% cumulative reduction [39]. The most recent work by Zielińska-Lipiec et. al presents the most representative evaluation of nanograined Alloy 2205 [31]. In this work, a common band-like structure was observed with no evidence of macroscopic shear banding even at high rolling reductions. Deformation induced austenite to ferrite transformations were observed, with dynamic recovery occurring in the ferrite. The austenite phase presented a Brass texture while the ferrite developed α- and γ-fibre components.

It is clear that DSS responds to severe plastic deformation in a variety of ways that are highly dependent on starting chemistry, rolling schedule, temperature, and lubrication. This paper does not aim to define this processing space. Rather the authors show results of using a dual phase material as a means to reduce the number of cycles needed to achieve FCC/BCC interfaces in nanolamellar composites. The use of accumulative roll bonding to quickly achieve reductions above 90% and the accompanying results have notably not been reported (to the authors knowledge). As a result, this work adds to both the body of literature concerning nanolamellar composites and that concerning severe plastic deformation of DSS.

2.0 EXPERIMENTAL METHODS

A nanolaminate structure of Alloy 2205, that began with equal proportions of austenite (51% volume fraction) and ferrite (49% volume fraction), was produced by accumulative roll bonding (ARB) and subsequent cold rolling at room temperature. The starting material consisted of a single plate of Alloy 2205 (4.76mm thick) purchased from Langley Alloys (Vancouver, WA, USA), with the composition listed in Table 1. Volume fraction of the austenite and ferrite phases in the starting material was confirmed via electron back scatter diffraction (EBSD) and neutron diffraction (NeD).

Table 1: Compositions of Alloy 2205 duplex steel, as defined by Langley Alloys.

	Fe	**C**	**Cr**	**Ni**	**Mo**	**N**	**Si**	**P**	**S**
at. %	bal.	<0.03	22-23	4.5-6.5	3.0-3.5	0.14-0.20	0.2-0.7	<0.03	<0.02

The material in this study began as 4.76 mm thick plate and is referred to as the 0% reduction condition. In order to promote bonding, a 5 min ultrasonic acetone bath and wire-brushing was performed prior to each roll bonding step. To create the initial bonded plate, two sections of plate material were stacked and given an 80.5% reduction in a single pass on a two-high rolling mill with 46 cm diameter rolls rotating at 38 cm/sec (Waterbury-Farrel, Brampton, Ontario, Canada), resulting in a two-layer (L=2) laminate structure. Previous work in accumulative roll bonding (ARB) has shown that a minimum of 50% rolling reduction is required to fully bond bulk material layers and was therefore the desired level of deformation during ARB [22]. ARB steps, after the noted surface preparation, was then used to produce the 80.5% and 92.5% reduced material. From here, sections of material were given additional cold-reductions (CR) resulting in 95% and 97% cumulative strain conditions, each with 8-layers (L=8). No heat treatments were applied at any point during the process. The change from ARB to cold rolling was due to the hardness of the material. In ARB ~50% reductions in a single pass are required to achieve bonding. With hard material this can damage the rolls. Due to the hardness observed, a decision was made to change to cold rolling to achieve finer length scales.

Sample preparation for EBSD consisted of mounting samples in two-part epoxy with the section plane oriented in the transverse direction (TD) or perpendicular to both ND and RD, grinding on SiC papers to 1200 grit, polishing to a 0.05 μm finish using colloidal alumina, followed by vibratory polishing with a 0.05 μm colloidal silica suspension. Preparation for S/TEM examination similarly consisted of grinding on SiC papers to reveal the TD to ~100 μm thick with a 600 grit finish, punching into 3 mm discs, and twin-jet electropolishing in a 10% perchloric, 45% acetic, 45% methanol (by volume) electrolyte at 45 mA, 15 V, -30 °C to electron transparency.

EBSD was performed on a FEI Inspect (FEI, Hillsboro, OR, USA) scanning electron microscope (SEM) using a TSL/EDAX Hikari EBSD camera and software (TSL, Draper, UT, USA) at 20 kV, a 50 μm objective aperture, and a 0.5 μm step size. Data cleanup consisted of a neighbor confidence index correlation (NCIC) cleanup with a minimum CI of 0.3, followed by a Neighboring Phase Correlation, with less than 15% of the total dataset being adjusted. S/TEM examination was conducted on a FEI Tecnai TF30 at 300 kV and FEI Titan image corrected 80-300 at 300 kV (FEI, Hillsboro, OR, USA).

NeD was conducted at the Los Alamos Neutron Science Center (LANSCE) using the HIPPO diffractometer [41-42]. Sample preparation consisted of cutting a ~1 cm^2 coupon from the rolled material at each reduction level to allow the ~10 mm diameter NeD spot size to provide a bulk measurement for each deformation step. The volume from the edges deformed during cutting is estimated to be less than 5% and deemed negligible. Diffraction data were acquired from five groups of detector panels at nominal diffraction angles of $2\theta = 144°$, 120°, 90°, 60°, and 39°. To increase pole figure coverage, measurements were taken for different rotations around the sample holder axis by 0°, 67.5° and 90° with respect to the beam. A Rietveld refinement employing the MAUD program [43] was performed against the resulting 135 neutron diffraction patterns per sample using the E-WIMV method with a 7.5° resolution in order to simultaneously fit all of the diffraction data and determine the orientation distribution function (ODF) of each sample [42,44]. In addition, the anisotropic crystallite size and broaden model of POPA [53] with an L_{max} of 6 was used to capture the (hkl) specific peak broadening. The MTEX texture analysis software was used for interpretation of the ODFs presented in this paper [44-45]. Adjustments for minor sample misalignments due to mounting inaccuracies were made using the MTEX orthorhombic symmetry search function *centerSpecimen* which aligns the material frame with the intrinsic orthorhombic symmetry of the ODF that arises during the rolling process. This procedure virtually aligns the sample frames during the data analysis enabling reliable comparisons between samples.

The evolution of mechanical properties was examined primarily using Rockwell hardness indentation on a Buehler Macromet 3 (Buehler, Lake Bluff, Illinois, USA). Approximate values of ultimate tensile strength (UTS) were calculated using an ASTM standard conversion table [68] and were verified for the 92.5% reduction condition using a conventional INSTRON 1125 screw-driven load frame (INSTRON, Norwood, MA, USA) at a strain rate of 10E-3 s^{-1}. The mini tensile geometry used in this study can be seen in Figure 1.

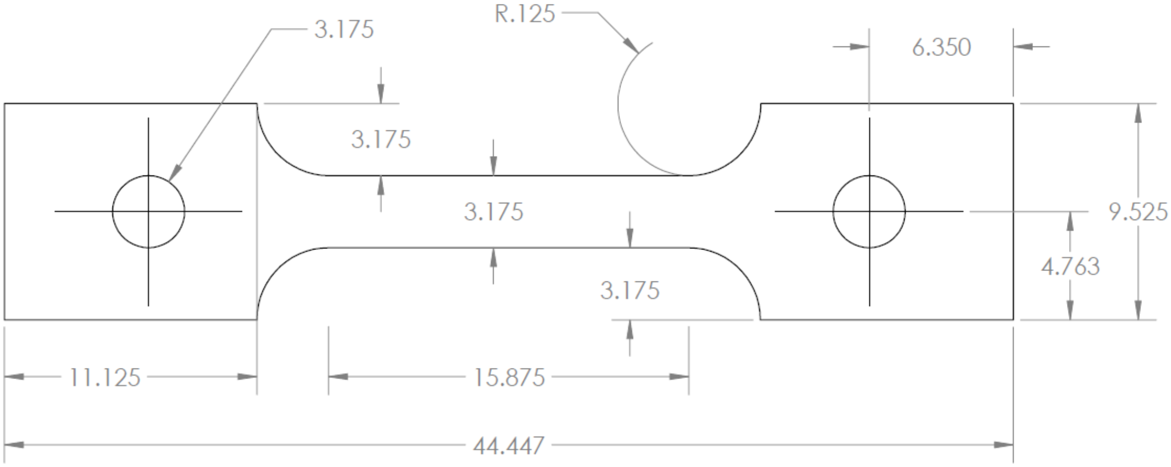

Figure 1: Specifications for the mini tensile specimens tested in this study. Units are in mm.

3.0 RESULTS

3.1 Grain Structure

The as-received plate material of Alloy 2205 exhibited a ferrite/austenite microstructure, as determined by High Pressure Preferred Orientation (HIPPO) neutron diffraction (NeD). EBSD results from the 80.5% reduction material (Figure 2) show a highly banded two-phase microstructure, often consisting of a single grain through individual layers. At this level of reduction, the layer/grain thickness is approximately 2 µm with alternating layers of austenite and ferrite. A high density of coincident site lattice (CSL) Σ3 boundaries were observed in the austenite phase, consistent with deformation twinning observed by other authors [46]. Conversely, no special boundaries were observed in the ferrite structure. It should be noted that no macroscopic or microscopic shear bands were observed during ARB processing but were later observed during traditional cold rolling beyond 92.5% reduction. Similarly, the twinning seen in Figure 2 was not observed during TEM investigations at reductions higher than 80.5%.

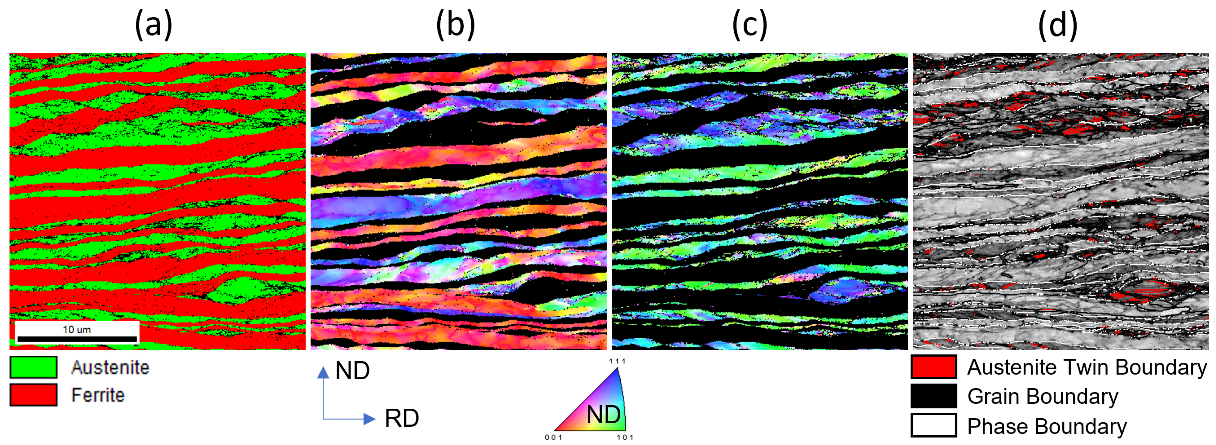

Figure 2: EBSD along the transverse direction for 80.5% reduction of Alloy 2205 showing (a) phase fraction map identifying austenite and ferrite, (b) inverse pole figure (IPF) map of ferrite, (c) IPF map of austenite and (d) an image quality map identifying twin boundaries in the austenite phase.

Bright Field TEM (BFTEM) examination of the (a-b) 92.5, (c-d) 95, and (e-f) 97% reduction materials are shown below in Figure 3. In all cases the spot diffraction patters are consistent an approximate Kurdjomov-Sachs (KS) orientation relationship between the austenite and ferrite. With rare exception, the morphology is highly layered in both EBSD and TEM studies and exhibits grains of austenite or ferrite with some dislocation content. This is indicated by both the contrast in BFTEM micrographs as well as the streaking in selected area electron diffraction (SAED) images. The TEM makes it clear that the grains are layer-like features elongated in the rolling direction and transverse direction. However, the small grain size makes it difficult to quantify how often a layer of austenite or ferrite consists of a single grain. This is why Table 2 reports results in terms of grain size as opposed to layer thickness. Note that evidence of localized shear banding was observed at 95 and 97.5% reduction. Observed areas of shear banding showed much finer grain sizes than the majority of grains observed in TEM. Reporting an approximate grain size in Table 2 is meant to convey the heterogeneity of the microstructure at these length scales. While the dislocation substructure was not identified through microscopy as a martensitic morphology, it is noted that the neutron diffraction results show an increase in ferrite volume fraction, indicating the presence of martensite. As was clearly shown by Rys et al., [51], martensite should form within the austenite with a KS relationship and thus a similar orientation to the ferrite. Differentiating between ferrite and martensite is challenging within diffraction and the development of martensite would be observed as an increase in ferrite volume fraction via bulk neutron diffraction measurements. However, due to increasing defect density with reduction, the isotropic thermal displacement (which is enhanced by defect density and must be refined [54]), the size-strain model, and texture contributions become increasingly correlated and the global quality metric response surface (i.e. Rietveld fit quality as a function of phase fractions) becomes flat. As a result, certainty in phase fraction decreases with reduction (see Appendix A and Section 4 for further discussion). In Table 2, best fit Rietveld estimates suggest an increase in ferrite of ~8% at 97% reduction and is consistent with martensitic transformation. This indicates that much of the contrast observed in BFTEM is likely due to dislocation content, but that some could be due to martensitic transformation. No obvious regions of martensite in austenite layers were observed during TEM, which also suggests low volume fractions of martensite.

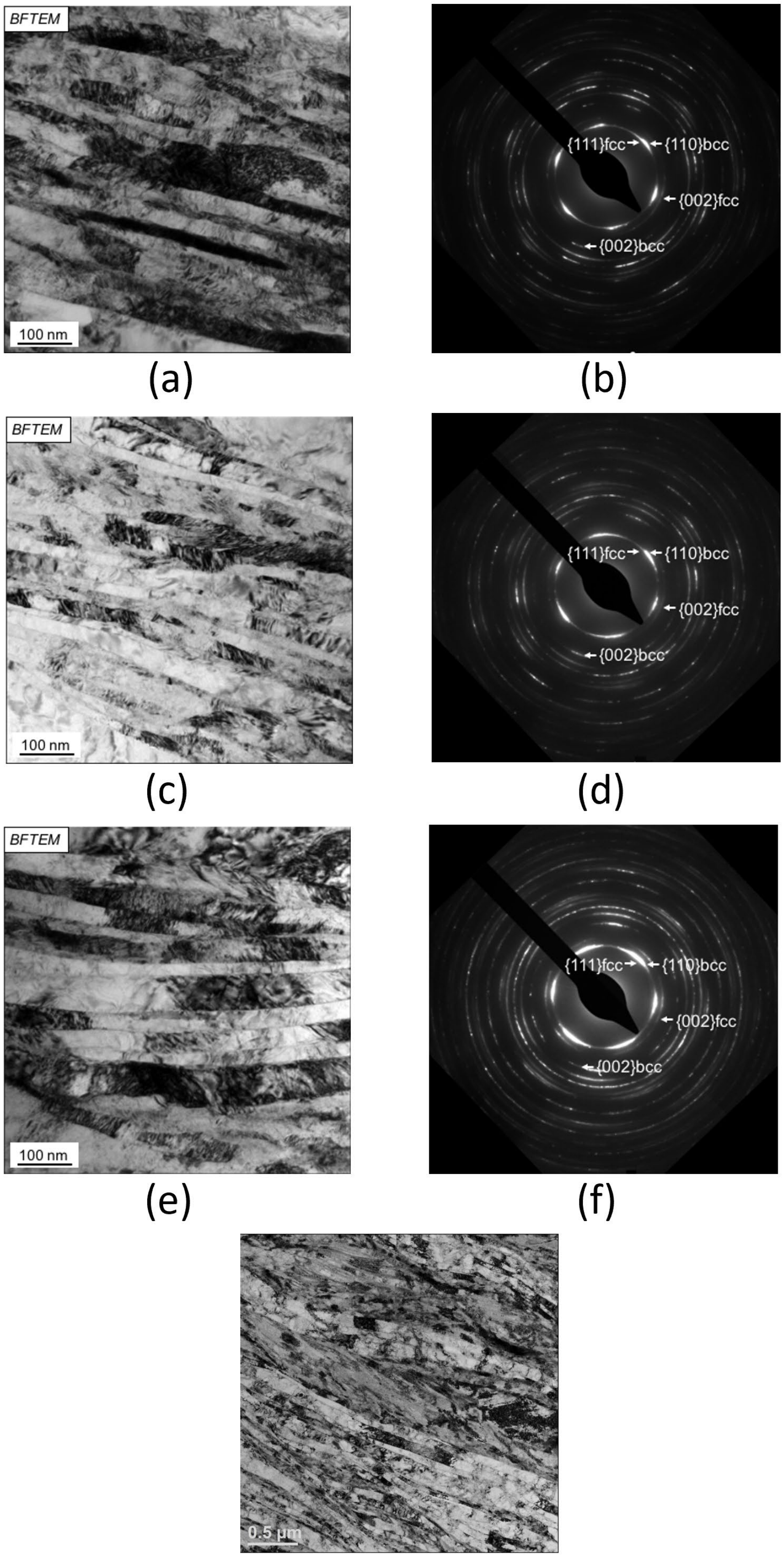
BFTEM
100 nm
{111}fcc
{110}bcc
{002}fcc
{002}bcc
BFTEM
100 nm
{111}fcc
{110}bcc
{002}fcc
{002}bcc
BFTEM
100 nm
{111}fcc
{110}bcc
{002}fcc
{002}bcc
0.5 μm

(a) (b)

(c) (d)

(e) (f)

(g)

Figure 3. BFTEM images and SAED patterns (B = $[011]_{fcc} \parallel [111]_{bcc}$) of Alloy 2205, showing the substructure evolution and a preference for near Kurdjumov-Sachs orientation relationships after (a-b) 92.5%, (c-d) 95%, and (e-f) 97% reduction. The viewing direction for the images is the the TD with the sectioned plane containing the sheet normal (ND) and rolling directions (RD). (g) Evidence of shear banding at 95% reduction.

3.2 Mechanical Properties

Rockwell hardness (HRC) shows a significant increase in hardness up to 92.5% reduction, after which no increase in hardness and by extensions UTS is observed. To verify the hardness estimates, a sample from the 92.5% material was taken for tensile testing, and the results (Figure 4) closely correlate with the hardness estimated from UTS. Note that Figure 4 shows that the material exhibits high tensile strength (~1439 MPa) with reasonable ductility. Furthermore, the hardness value obtained from the 92.5% is consistent with results from other authors that reported between 42 and 47 HRC for rolling reductions between 85% and 96.6%, despite widely varying quantities of reported transformed martensite [38,52]. A summary of the mechanical properties for the various rolling reductions can be found in Table 2.

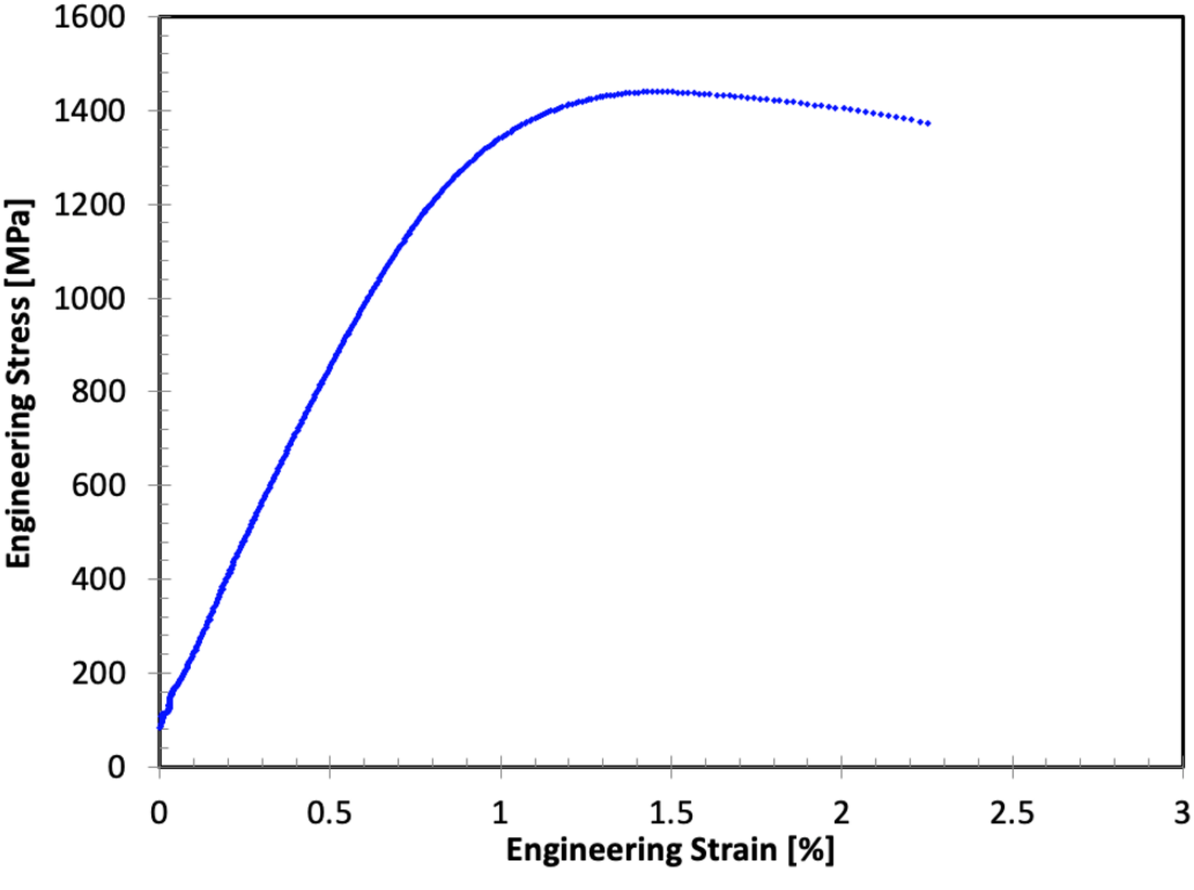

Figure 4: Tensile stress-strain curve of the 92.5% reduction material. Rockwell C predicts an approximate UTS of 1480 MPa [68], and the experimentally observed value is 1439 MPa.

Table 2: Summary of mechanical properties for Alloy 2205 as a function of cold reduction.

% Reduction	Grain Thickness (h)	HRC	UTS-HRC$^{\#}$ (MPa)	UTS (MPa)	% Ferrite/Martensite*	# ARB Layers
0	---	20	760	---	49	1
80.5	1-2 μm	40	1250	---	49	2
92.5	100 nm	45	1480	1439	50	8
95	< 100 nm	45	1480	---	52	8
97	< 100 nm	44	1430	---	57	8

*Percent ferrite as determined by neutron diffraction and analysis in Appendix 1. $^{\#}$[68]

3.3 Texture

This section details the various texture components within the austenite and ferrite phases as determined by HIPPO neutron diffraction. As seen in Figure 5, the ferrite phase of this dual-phase structure in the as-received condition (0%) contains a strong rotated cube component (10.45 times random), along with a very minor Goss component. With increasing deformation, we see the development of α- and y-fiber texture fibers and with continued intensities at the rotated cube orientation, but no presence of a Goss component. The austenite phase in the as-received (0%) condition exhibits weak textures with small amounts of bias (~2 times random) towards cube, copper, and brass textures. With increasing deformation, we see the disappearance of the cube, S, Dillamore, and copper components, transitioning into a mixed brass and Goss texture.

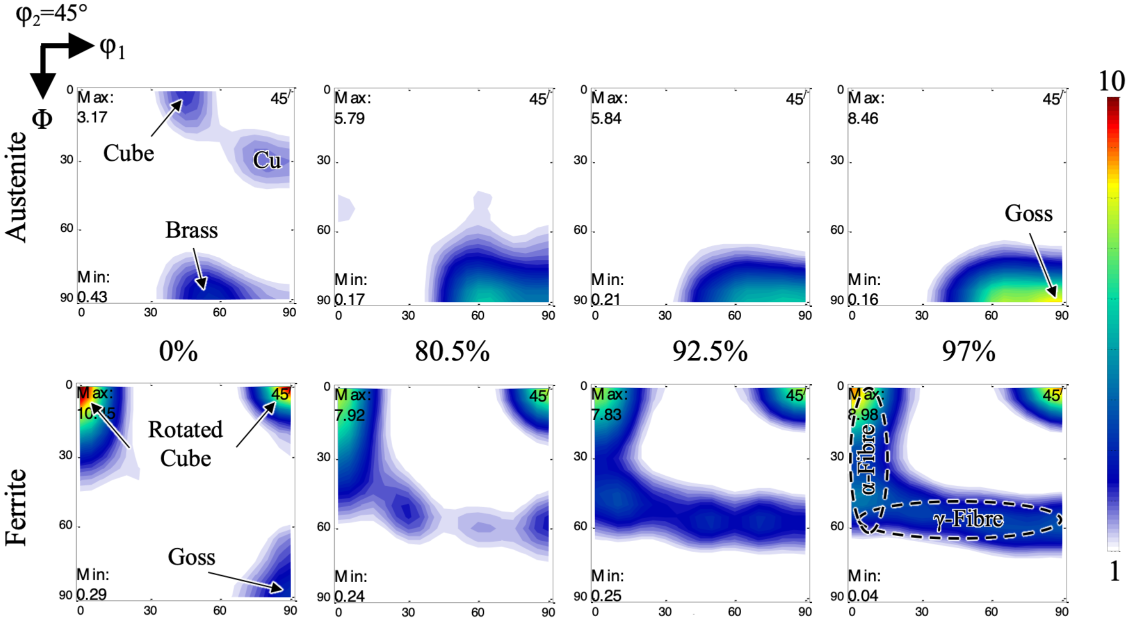

Figure 5: Texture evolution of the austenite (top) and ferrite (bottom) phases with increasing rolling reduction, shown by the orientation distribution function (ODF) 2D slices where $\varphi_2 = 45°$.

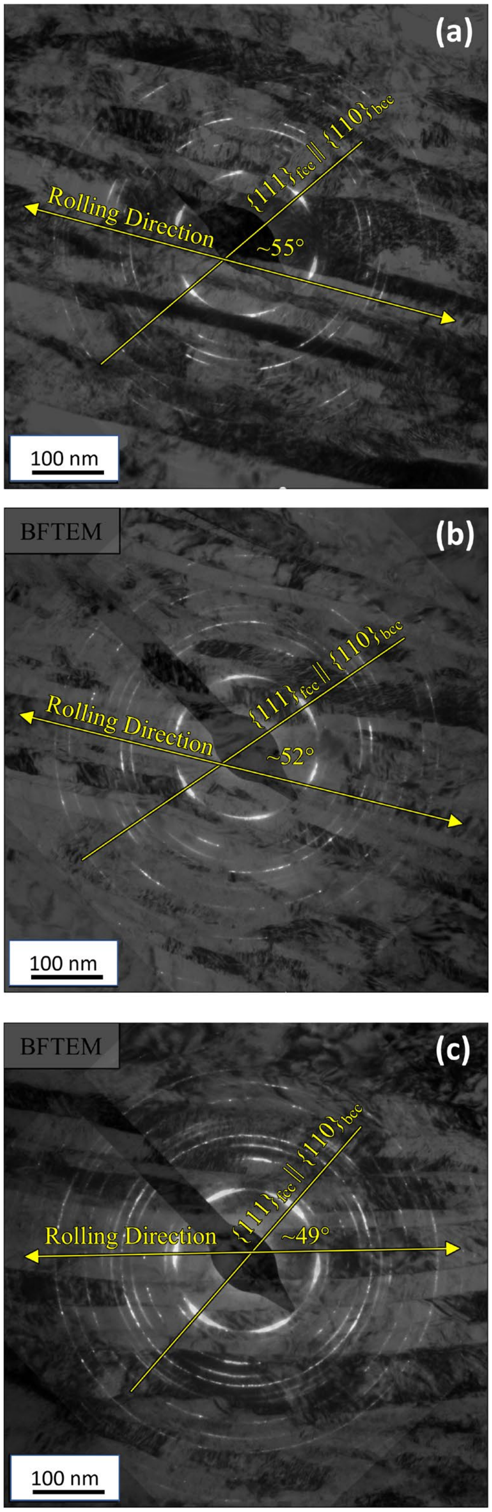

Figure 6: TEM SAED overlaid on the BFTEM image for the (a) 92.5%, (b) 95%, and (c) 97% reduction material, showing the deviation between the Kurdjumov-Sachs habit plane and the interphase interface normal of 30-40°.

4.0 DISCUSSION

As stated in the introduction, the over-arching purpose of this manuscript is to identify differences in behavior between DSS2205 that has undergone ARB and the well-studied Cu/Nb system.

Single phase rolling of austenite to 92% provided textures consisting of copper, cube, and brass indicating that the presence of the ferrite phase did affect the deformation of the austenite phase [34]. The resultant texture for austenite in the composite in this study showed strong brass and Goss components to the exclusion of other orientations. This is consistent with the observed stable near-KS interface structure shown in Figure 6.

The presence of the ferrite phase in the composite and the associated co-deformation condition, leads to texture evolution and the grain orientations that provide a near KS relationship that are stable with continuing deformation. Unlike single phase ferrite, the rotated cube component orientation was prominent in the ferrite of this composite and is consistent with literature comparing rolled duplex steel with rolled single phase ferrite [50]. The K-S interface relationship is similar to that observed in Cu/Nb which also maintained this orientation relationship at the interface from macroscale down to nanoscale [22, 49]. Figure 6 also clearly shows that the shared K-S plane (bcc (110) / fcc (111) is rotated 30 to 40° away from the interface normal. The offset observed in Cu-Nb was on the order of a few degrees and was shown to be defined by the creation of aligned slip planes after twinning in the Cu phase [55].

BF TEM exhibited no evidence of stress-induced martensite contrary to reports of other authors [38-40]; however, bulk neutron diffraction measurements identified that up to 8% martensite could be present. Appendix A discusses a parametric study of weight fraction versus the increasing dislocation density in ferrite and austenite with rolling reduction. This methodology allows a determination of the range of likely martensitic fractions while significant correlation in Rietveld parameters exist. Since recovery is not expected, the dislocation content in the austenite phase and Rietveld fit quality suggests 4.5% to 8% martensite is possible. Literature indicates that the transition to martensite can be observed as the Brass texture component in the austenite phase decreases. Observed transitions in peak intensity from Brass and Goss to Goss only were seen to be driven by the instability of the brass component and transformation to strain induced martensite [47]. Figure 7 provides the alpha fiber intensities observed in neutron diffraction. It is clearly shown that Goss strengthens at a faster rate than Brass, perhaps because of martensitic transformation. In addition, literature indicates that 12% of the austenite was observed to transform to martensite at rolling reductions of 85% for DSS2205 as observed by neutron diffraction for cold rolling without bonding [38]. Higher amounts have been seen in similar grades of DSS such as S31803 [52] in which ~ 28% of austenite had transformed at 92.5% reduction and ~50% of austenite had transformed at 96.6%. The austenite to martensite transformation accommodates an equivalent strain on the order of 20% and given the low volume fraction of martensite observed here, martensite does not contribute significantly to the deformation. When this result is coupled with the minimal shear banding and austenite twinning at reductions beyond 80.5% (see Figure 2), it is apparent that slip remains the dominant deformation mechanism even at layer thicknesses below 100 nm and strain induced martensite also assists to a much lesser extent with deformation. The Cu orientation in Cu/Nb, on the other hand, began to undergo twinning at low length scales as an alternative to slip and this was observed by clear texture changes in the material at length scales below 200 nm [48].

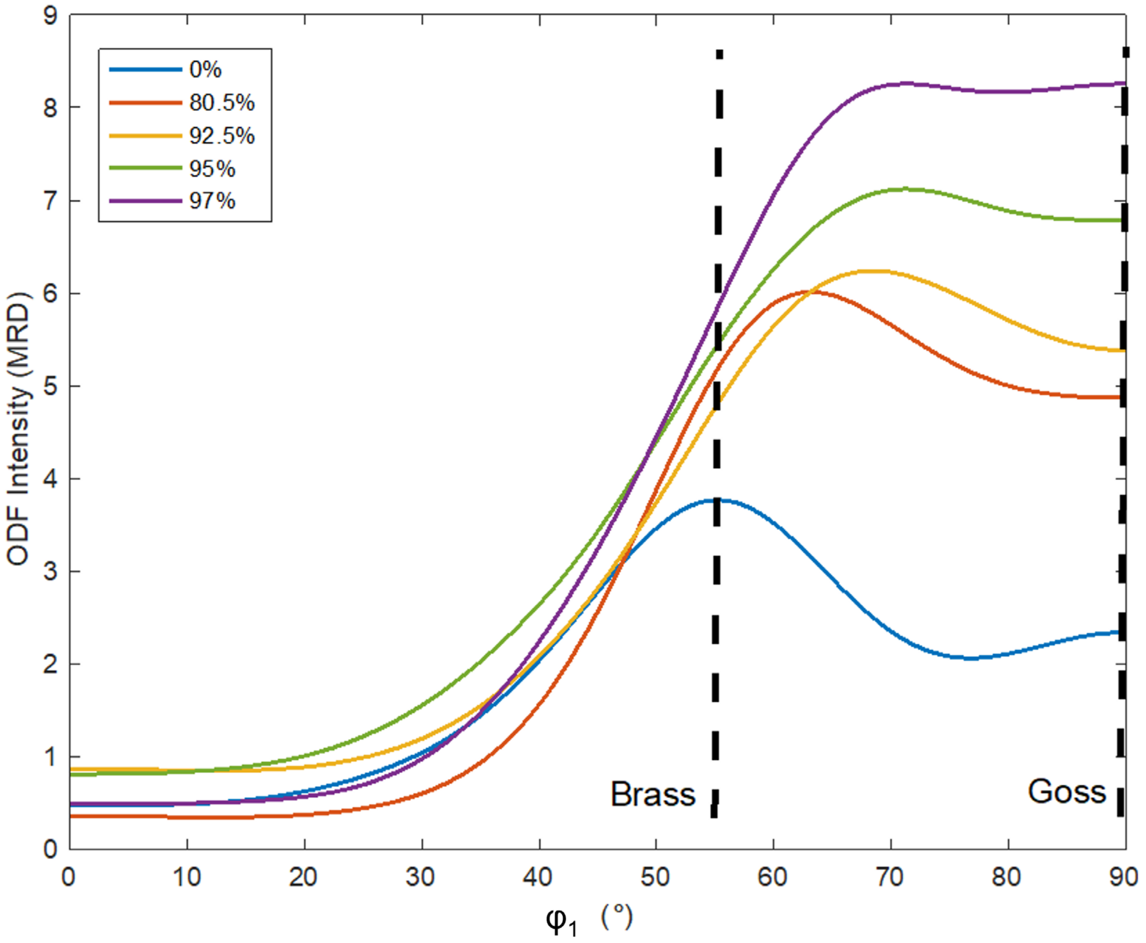

Figure 7: Alpha fiber plot for FCC austenite showing stability of brass orientation and increase in Goss intensity with increases in rolling reduction.

The chemical and mechanical driving force associated with the austenite to martensite transformation as described by Patel and Cohen is augmented by both the stress state and temperature [56]. It is important to note that small changes in chemistry are present between the starting material in this study and the cited literature which prevents direct comparisons as chemical changes affect the energetics of martensitic formation. In austenitic stainless steels it is well known that for the transformation to occur, the mechanical driving force has to increase in magnitude if the temperature is raised e.g. due to the large rolling reduction of an ARB step [57, 58]. As a general rule, most of the mechanical energy during rolling is dissipated through adiabatic heating of the sample and in the present study it is expected that the sample would heat significantly given the strain magnitude, strain-rate, and literature for austenitic stainless steels [59, 60]. In addition, changing the deformation mode or ratio of modes is known to introduce a stress dependence on the kinetics of the transformation [58, 60, 61]. Thus, it is not surprising that large reduction ARB would significantly alter the driving forces for martensite transformation and by extension observed martensite fractions from other DSS2205 rolling works [38-40] and that of cold rolling with smaller rolling reduction would be more favorable for transformation of austenite to martensite – whether that is due to strain and stress components changing from reduced roll contact area or due to reduced adiabatic heating [62].

Hardness of the duplex structure saturated at 92.5% rolling reduction with a measured hardness of 45 HRC (~1430 MPa). Verification of hardness values via tensile testing were performed on the 92.5% reduction material and correlated well. Unlike the aforementioned FCC/BCC composites, layer/grain thickness did not continue to diminish with increasing reduction above 92.5% (see Table 2). Unlike Cu/Nb, for instance, the layers are not continuous through the length of the rolled plate. This could allow for non-uniform deformation across the plate thickness which would allow some overall height reduction with no commensurate layer thickness reduction. In addition, unlike Cu/Nb, shear banding was observed for deformations above 92.5%. The localized nature of the shear bands could allow for an increase in overall plate length without leading to large changes in texture or observed layer thickness. Finally, the limited area observable in TEM showed variations in grain thickness similar to that seen in Figure 2. This stemmed from the non-uniform grain sizes that were present in the initial material. Grain measurements with limited statistics pointed towards areas where grains were 10 nm in thickness and as high as 200 nm in thickness at 95% reduction. It is entirely likely that all three of these listed effects, in combination, lead to the lack of a uniform observed layer thickness decrease with reductions beyond 92.5%.

The lack of increase in hardness above 92.5% reduction can be explained as localized shear banding, discontinuous layers with non-uniform starting thicknesses, and martensitic transformation, leaving the bulk of the microstructure in a similar configuration as seen at 92.5%. When shear banding is observed in austenitic and duplex stainless steels, the martensite is initially observed near the shear bands [64,65]. The onset of shear banding and the transformation of martensite beginning simultaneously is consistent with literature. This provides a strong indication that this change in mechanism from co-deforming layers to shear banding is a result of any of these three options; (a) the change in processing from roll bonding to rolling; (b) the mismatch in flow stress has become too significant and leading to layer pinch-off; or (c) twinning as a mechanism for accommodating plasticity has become exhausted. In the Cu/Nb system, co-deformation was maintained to the nanoscale even when adjustments from roll bonding to rolling to cross-rolling were made [63]. Notably, duplex steel is observed to undergo extensive shear banding during cold rolling [65]. The transition to shear banding coupled with martensitic transformation upon resumption of reduced reductions via cold rolling could be indicative that ARB provides certain advantages in delaying or deactivating certain plasticity accommodating mechanisms. Roll bonding, as noted earlier, was halted because the material was unable to undergo a 50% reduction with the mills available at LANL. In the future, performing three consecutive ARB steps without the use of cold rolling and comparing could provide a comparison to this work and determine if (a) leads to the onset of shear banding. The mismatch in flow stress would be challenging to determine as there are few ways to accurately measure the flow stress in grains that are ≤ 100 nm in a dimension. Twinning in austenite in DS2205 has been observed to cease as a deformation mechanism as austenite grain sizes are reduced to 100 to 200 nm [66]. It was noted that this arose as a result of the diminished length scale of the grains and leads to the onset of dislocation mediated plasticity and shear banding. It is, therefore, inconclusive, if one or a combination of (a), (b), and (c) lead to the onset of shear banding.

Hardness values are observed to be saturated consistent with the observed, average grain size. Further ARB of the DSS 2205 beyond 92.5% was unsuccessful as the material was too hard to achieve the required reductions for bonding with the current equipment. Cold rolling of the material beyond 92.5% leads to minimal layer thickness reduction, limited texture evolution, and no increase in strength (but increase in martensite fraction). It is unclear whether this saturation of several microstructural quantities would change if further roll bonding was performed using 92.5% reduction. Interestingly and perhaps coincidently, it is only upon rolling without ARB that the austenite to martensite phase transformation appears in bulk Neutron diffraction. This may indicate that shear and temperature play an important part in the transformation of austenite to martensite when sample thickness diminishes and rolling reductions are reduced. It is also possible that the lack of continuous layers (despite their elongated structure) is responsible for the saturation of mechanical properties, grain size, and texture. A UTS of 1430 MPa, however is extremely high for DSS 2205 [29] and this was accomplished with only two roll bonding passes. The route shown in this manuscript points to a rapid way to both refine and strengthen DSS 2205. It also shows that further reductions beyond 92.5% do not lead to an increase in strength or hardness but deformation mechanisms such as slip, martensitic transformation, and shear banding allow for continued texture development and overall plate thickness reduction.

5.0 CONCLUSIONS

In summary, DSS 2205 was processed with ARB and cold rolling to reductions of 97%. Nanoscale layers below 100 nm in thickness were created in only two ARB steps and the material exhibited strengths greater than 1400 MPa in ultimate tensile strength. This methodology is a rapid way to produce nanoscale DSS2205 with high strength. As with other FCC/BCC composites processed by ARB to the nanoscale, the texture of both the FCC austenite and BCC ferrite were observed to strengthen around a few specific orientations. In addition, these orientations were different from those expected for single phase rolling reductions of the constituent phases indicating that the co-deformation condition exerted influence on orientation evolution. Changes in expected texture were also observed in Cu/Nb as compared to single phase rolling to high reductions. The strong textures developed result in many phase interfaces exhibiting an orientation relationship that is close to the KS orientation relationship, which is also consistent with Cu/Nb, albeit with a different offset from the interface normal. No twinning was observed in FCC austenite upon reaching the nanoscale despite its propensity and observed history of twinning. This is in contrast to the twinning observed in nanoscale Cu in Cu/Nb multilayers [48]. It is likely that the austenite's ability to twin was exhausted during the early stages of ARB as Figure 2 clearly shows the expected, high amounts of twinning and texture results indicate a diminishment in Cu, S, and Dillamore texture components which are conducive to twinning in fcc materials. Martensitic transformation was observed via neutron diffraction and, importantly, quantified with amounts of martensite much less than those published in literature during conventional rolling of DSS2205 and similar grades of DSS. Finally, the grain size and hardness were observed to saturate above 92.5% reduction coupled with the onset of shear banding. Finally, it appears that the roll bonding of an industrial relevant FCC/BCC composite provides a rapid way to achieve small length scales with high strength lending credibility to the transition of the observed properties in model systems like ARB Cu/Nb towards industrially relevant starting materials. Neutron diffraction indicates that a martensitic transformation of ~8% is required in order to provide realistic trends in dislocation density development and achieve high quality fits.

6.0 ACKNOWLEDGMENTS

This work was supported by the U.S. Department of Energy through the Los Alamos National Laboratory. Los Alamos National Laboratory is operated by Triad National Security, LLC, for the National Nuclear Security Administration of the U.S. Department of Energy under contract 89233218CNA000001. This work was funded through Los Alamos National Laboratory Directed Research and Development (LDRD) projects ER20200375 and DR20200182. This work has benefitted from the use of the Los Alamos Neutron Science Center (LANSCE) at LANL. DJS and SCV gratefully acknowledge funding from Information Science and Technology Institute and the Institute for Materials Science for support in data analysis automation applied for this project.

7.0 CONFLICT OF INTEREST STATEMENT

On behalf of all authors, the corresponding author states that there is no conflict of interest.

8.0 REFERENCES

1. P.D. Funkenbusch and TH Courtney, , Acta Metall., 33, (1985).
2. H.P. Wahl and G. Wassermann, Z. Metallk., 61, (1970).
3. G. Frommeyer and G. Wassermann, Acta Metall., 23 (1975).
4. CL Trybus and WA Spitzig, Acta Metall., 37 (1989) 1971-1981.
5. WA Spitzig, AR Pelton, FC Laabs, Acta Metall., 35 (1987) 2427-2442.
6. A Misra, M Verdier, YC Lu, H Kung, TE Mitchell, N Nastasi, JD Embury, Scripta Mat., 39 (1998) 555-560.
7. JT Wood, AJ Griffin Jr, JD Embury, R Zhou, M. Nastasi, M. Veron, Journal of the Mechanics and Physics of Solids, 44 (1996) 737-750.
8. K Adachi, S Tsubokawa, T Takeuchi, HG Suzuki, Journal of the Japan Institute of Metals, 61 (5) (1997) 397-403.
9. TE Mitchell, YC Lu, AJ Griffin, M Nastasi, H Kung, J. Am. Ceram. Soc., 80 (1997) 1673-1676.
10. SA Barnett and M Shinn, Ann. Rev. Mater. Sci., 24 (1994) 481-511.
11. A Misra and R. Hoagland, Jour. Mater. Res., 20 (2005) 2046-2054.
12. JS Carpenter, SJ Zheng, RF Zhang, SC Vogel, IJ Beyerlein, NA Mara, Philos. Mag., 93 (2013) 718-735.
13. JS Riano, and AM Hodge, Scripta Mater. 166 (2019) 19-23.
14. WF Yang, IJ Beyerlein, QQ Jin, HL Ge, T Xiong, LX Yang, JC Pang, YT Zhou, XH Shao, B Zhang, SJ Zheng, XL Ma, Scripta Mater. 166 (2019) 73-77.
15. WZ Han, MJ Demkowicz, NA Mara, EF Fu, S Sinha, AD Rollett, YQ Wang, JS Carpenter, IJ Beyerlein, A Misra, Adv. Mater. 25 (2013) 6975-6979.
16. LF Zeng, P Fan, LF Zhang, R Gao, ZM Xie, QF Fang, XP Wang, DQ Yuan, T Zhang, CS Liu, J. Nucl. Mater., 508 (2018) 354-360.
17. WZ Han, NA Mara, YQ Wang, A Misra, MJ Demkowicz, J. Nucl. Mater., 452 (2014) 57-60.
18. HPA Ali, I Radchenko, N Li, A Budiman, Mater. Sci. Eng. A 738 (2018) 253-263.
19. J. Wang, Q Zhou, S Shao, A Misra, Mater. Res. Lett., 5 (2017) 1-19.
20. M. Ardeljan, M Knezevic, T Nizolek, IJ Beyerlein, NA Mara, TM Pollock, Int. J. Plast. 74 (2015) 35-57.
21. X He and Y Shen, JOM, 67 (2015) 1486-1490.

22. JS Carpenter, SC Vogel, JE LeDonne, DL Hammon, IJ Beyerlein, NA Mara, Acta Mater., 60 (2012) 1576-1586.
23. LF Zeng, R Gao, ZM Xie, S Miao, QF Fang, XP Wang, T Zhang, CS Liu, Sci. Rep. 7 (2017) 40742.
24. LF Zeng, R Gao, QF Fang, XP Wang, ZM Xie, S Miao, T Hao, T Zhang, Acta Mater. 110 (2016) 341-351.
25. JS Carpenter, T Nizolek, RJ McCabe, M Knezevic, SJ Zheng, BP Eftink, JE Scott, SC Vogel, TM Pollock, NA Mara, IJ Beyerlein, Acta Mater., 92 (2015) 97-108.
26. MM Mahdavian, L Ghalandari, M Reihanian, Mater. Sci. Eng. A, 579 (2013) 99-107.
27. YF Sun, N Tsuji, H Fujii, FS Li, J. Alloys and Comp., 504 (2010).
28. Y Saito, H Utsunomiya, N Tsuji, T Sakai, Acta Mater. 47 (1999) 579-583.
29. *Practical Guidelines for the Fabrication of Duplex Stainless Steels*. International Molybdenum Association, 2009.
30. J. Hay, *Appl. Note*, pp. 1–4.
31. J. Ryś and A. Zielińska-Lipiec , Int. J. Mater. Res., 106, (2015) 771-781.
32. R. Shashanka and D. Chaira, Powder Technol., 259, (2014) 125-136.
33. R. Shashanka,and D. Chaira, Mater. Char., 99, (2015) 220-229.
34. J. Keichel, J Foct, G Gottstein, ISIJ Int., 43, (2003) 1781-1787.
35. J. Ryś and M. Witkowska, Arch. Metall. Mater., 55, (2010) 733-747.
36. J. Ryś and A. Zielińska-Lipiec Arch. Metall. Mater., 57, (2012) 1041-1053.
37. J. Hamada and N. Ono, Mater. Trans., 51, (2010) 644-651.
38. M. Breda, K Brunelli, F Grazzi, A Scherillo, I Calliari, Metall. Mater. Trans. A*,* 46, (2015) 577-586.
39. N. Akdut and J. Foct, ISIJ Int., 36, (1996) 883-892.
40. JL Lv, TX Liang, C Wang, LM Dong, Mater. Sci. Eng. C, 62, (2016) 558-563.
41. HR Wenk, L Lutterotti, SC Vogel, Nucl. Instrum. Methods. Phys. Res. Sect. A, 515 (2003) 575-588.
42. SC Vogel, C Hartig, L Lutterotti, RB Von Dreele, HR Wenk, DJ Williams, Powder Diff., 19 (2004) 65-68.
43. L. Lutterotti, S Matthies, HR Wenk, AS Schultz, JW Richardson, J. Appl. Phys., 81, (1997) 594-600.
44. R. Hielscher and H. Schaeben, J. Appl. Crystallogr., 41, (2008) 1024-1037.
45. NC Popa, J. Appl. Cryst., 31 (1998) 176-180.
46. F. Bachmann, R. Hielscher, and H. Schaeben Solid State Phenom., 160, (2010) 63.
47. Standard Test Methods and Definitions for Mechanical Testing of Steel Products, ASTM Standard A370-21, American Society for Testing and Materials, (2021).
48. G. Krauss, *Steels: Processing, Structure, and Performance*, 4th ed. Materials Park: ASM International, 2005.
49. J. Ryś, G. Cempura, , Mater. Sci. Eng. A 700 (2017) 656-666.
50. K Zhang, IV Alexandrov, AR Kilmametov, RZ Valiev, K Lu, , J. of Phys. D: Appl. Phys., 30 (1997).
51. S.S.M. Tavares, MR da Silva, JM Pardal, HFG Abreu, AM Gomes, J. Mater. Process. Tech., 180 (2006) 318-322.
52. J. Capek, M Cernik, N Ganev, K Trojan, J Nemecek, K Kolarik, IOP Conf. series: Materials Science and Engineering 375 (2018) 012025.

53. JS Carpenter, RJ McCabe, JR Mayeur, NA Mara, IJ Beyerlein, Adv. Eng. Mater., 17 (2015) 109-114.
54. SJ Zheng, JS Carpenter, RJ McCabe, IJ Beyerlein, NA Mara, Sci. Rep. 4 (2014) 4226.
55. D Raabe, Acta Mater., 45 (1997) 1137-1151.
56. RJ McCabe, IJ Beyerlein, JS Carpenter, NA Mara, Nat. Comm., 5 (2014) 3806.
57. JR Patel, M Cohen, Acta Metallurgica, 1, (1953) 531-538.
58. CB Finfrock, D Bhattacharya, BNL McBride, TJ Ballard, AJ Clarke, KD Clarke, JOM, 74 (2022) 506-512.
59. LE Murr, KP Staudhammer, SS Hecker, Metallurgical Transactions A, 13 (1983) 627-635.
60. J Talonen, H Hanninen, P Nenonen, G Pape, Metallurgical and Materials Transactions A, 36 (2005) 421-432.
61. SS Hecker, MG Stout, KP Staudhammer, JL Smith, Metallurgical Transactions A, 13 (1982) 619-626.
62. AM Beese, D Mohr, Acta Materialia, 59 (2011) 2589-2600.
63. T Inoue, edited by David Moratal. London: IntechOpen, 2010. 10.5772/10233.
64. G. Sun, L. Du, J. Hu, B. Zhang, Mater. Char., 159 (2020) 110073.
65. G. Gianini Braga Maria, D. Gomes Rodrigues, E. Tadeu Fraga Freitas, D. Brandao Snatos, Mater. Lett., 234 (2019) 283.
66. JS Carpenter, RJ McCabe, SJ Zheng, TA Wynn, NA Mara, IJ Beyerlein, Met. Mater. Trans. A 45:4 (2014) 2192-2208.
67. M. Ma, H. Ding, Y. Huang, C.W. Tian, T.G. Langdon, Crystals, 10 (2020) 1138.
68. GK Williamson, RE Smallman, Philosophical Magazine, 1 (1956) 34-46.

9.0 APPENDIX A

During Rietveld refinement of neutron diffraction patterns collected at HIPPO, model parameters for size and strain, isotropic thermal displacement parameter (Biso), phase fractions, and texture must be refined among other standard variables such as lattice parameters, background and intensity scaling to model diffraction pattern features. With increased deformation level, there is an observed increase in Biso as observed in other extreme plastic deformation literature [54]. The ratio of Biso of two phases is moderately correlated with the volume fraction and is generally fixed to well accepted values for accurate phase fractions. However, with increased dislocation content this Biso ratio results in suboptimal diffraction pattern fits. In addition, the Biso also becomes correlated with the size and strain model and the signature of phase fraction in the global goodness of fit parameter Rwp becomes increasingly insensitive to small changes in phase fractions with rolling reduction. A general rule of thumb is to use details of difference curves to inform appropriate model selection, but the correlations result in similar pattern fit quality upon inspection for different phase fractions. For martensite transformed from a low carbon austenite, the BCT martensite structure is not distinguishable from the BCC ferrite diffraction pattern, thus it is not obvious if any Martensite has formed at first inspection of the Rietveld fits.

To address these uncertainties, a systematic study of the correlations (summarized in Figure A1) is performed by fixing the volume fraction of ferrite at various levels and refining Biso, texture, and the size-strain model. The most interesting of the trends in parameters is arises from the size-strain model. The POPA anisotropic size-strain broadening model was reduced in MAUD to an isotropic equivalent crystallite size, D, and isotropic equivalent microstrain, ϵ. Dislocation density estimates using the peak broadening analysis of Williamson and Smallman [67] are calculated as:

$$\rho = \sqrt{\frac{3k\epsilon^2}{D^2b^2}} \tag{A.1}$$

where k is an unknown material constant taken as unity and b is the burgers vector magnitude taken as $\frac{\sqrt{3}}{2}a$ where is a is the lattice parameter of the phase. While the magnitude of this estimate may be incorrect, the trends should be relevant. The dislocation density of austenite is not correlated to volume fraction of ferrite up to 95% reduction while after 80.5% reduction, there is a correlation in the ferrite dislocation density. Most notably, the second ARB step does not appreciably increase the dislocation density in either phase, while it appears to increase substantially from ARB quantities when cold rolling is performed. Also evident is that the dislocation density of Austenite becomes highly correlated with the volume fraction of ferrite at 97% reduction. Assuming no recovery causing a decrease in dislocation content, then the volume fraction of ferrite has likely increased above 53.5% and an upper limit from pattern fit inspection can be utilized to establish an upper boundary of ~57% volume fraction of ferrite with approximately 8% of ferrite being martensite transformed from austenite.

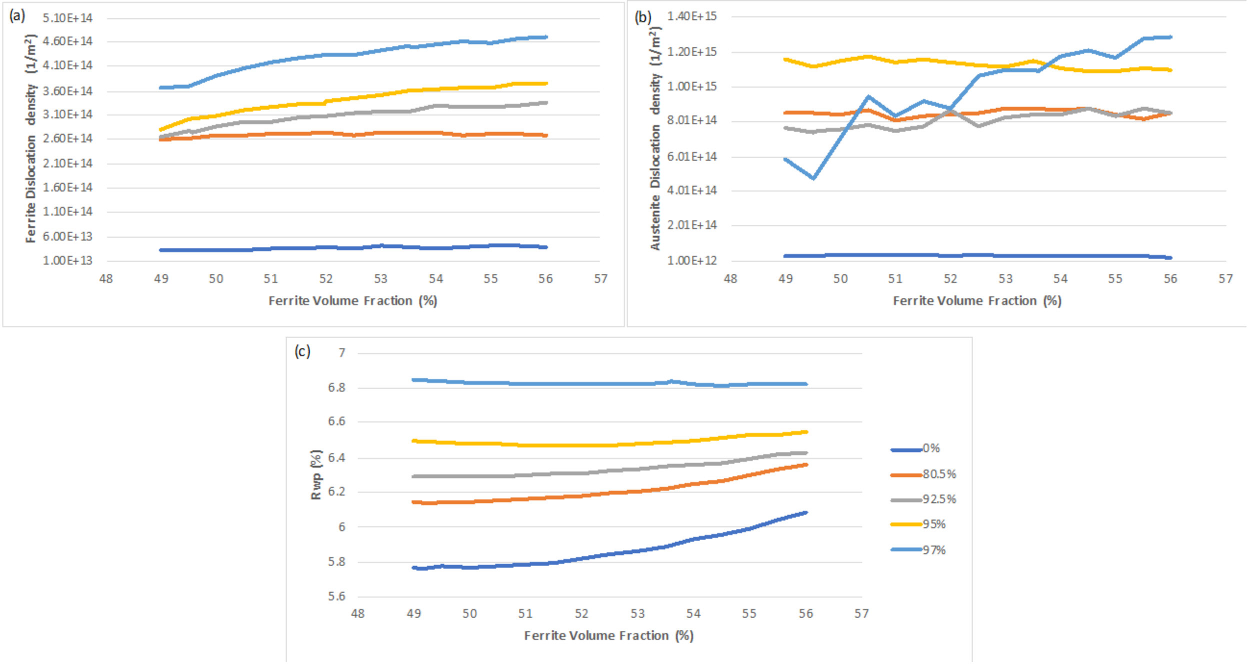

Figure A1: Summary of Rietveld parametric study of dislocation content in (a) ferrite and (b) austenite and (c) global refinement quality Rwp trend as a function of ferrite volume fraction. Ferrite volume fraction above 49% represent austenitic transformation to martensite.